The role of viscous magma mush spreading in volcanic flank motion at Kīlauea Volcano, Hawai'i

C. Plattner,[1,2,3] F. Amelung,[1] S. Baker,[1] R. Govers,[4] and M. Poland[5]

Received 30 August 2012; revised 21 February 2013; accepted 17 April 2013; published 16 May 2013.

[1] Multiple mechanisms have been suggested to explain seaward motion of the south flank of Kīlauea Volcano, Hawai'i. The consistency of flank motion during both waxing and waning magmatic activity at Kīlauea suggests that a continuously acting force, like gravity body force, plays a substantial role. Using finite element models, we test whether gravity is the principal driver of long-term motion of Kīlauea's flank. We compare our model results to geodetic data from Global Positioning System and interferometric synthetic aperture radar during a time period with few magmatic and tectonic events (2000–2003), when deformation of Kīlauea was dominated by summit subsidence and seaward motion of the south flank. We find that gravity-only models can reproduce the horizontal surface velocities if we incorporate a regional décollement fault and a deep, low-viscosity magma mush zone. To obtain quasi steady state horizontal surface velocities that explain the long-term seaward motion of the flank, we find that an additional weak zone is needed, which is an extensional rift zone above the magma mush. The spreading rate in our model is mainly controlled by the magma mush viscosity, while its density plays a less significant role. We find that a viscosity of 2.5×10^{17}–2.5×10^{19} Pa s for the magma mush provides an acceptable fit to the observed horizontal surface deformation. Using high magma mush viscosities, such as 2.5×10^{19} Pa s, the deformation rates remain more steady state over longer time scales. These models explain a significant amount of the observed subsidence at Kīlauea's summit. Some of the remaining subsidence is probably a result of magma withdrawal from subsurface reservoirs.

Citation: Plattner, C., F. Amelung, S. Baker, R. Govers, and M. Poland (2013), The role of viscous magma mush spreading in volcanic flank motion at Kılauea Volcano, Hawai'i, *J. Geophys. Res. Solid Earth*, *118*, 2474–2487, doi:10.1002/jgrb.50194.

1. Introduction

[2] Spreading and landsliding are common phenomena at volcanoes worldwide [*Borgia et al.*, 2000; *McGuire*, 2006], with the Hawaiian Islands, and particularly Kīlauea Volcano, providing the type examples (Figure 1) [*Swanson et al.*, 1976; *Moore et al.*, 1994]. Seaward motion of Kīlauea' south flank at rates of many cm/yr has been recognized from the analysis of trilateration and Global Positioning System (GPS) data over the past several decades, with the volcano's rift zones acting as the boundary between the mobile south flank and fixed north flank [*Swanson et al.*, 1976; *Delaney et al.*, 1993; *Owen et al.*, 1995; *Cayol et al.*, 2000; *Owen et al.*, 2000a; *Miklius et al.*, 2005]. The structure of the south flank is comparable to an active landslide [*Moore et al.*, 1989], including normal faults (Koa'e and Hilina Pali fault systems) and a subhorizontal basal décollement [*Lipman et al.*, 1985; *Denlinger and Okubo*, 1995]. Gravitational wedge instabilities, however, are an unlikely cause for flank instability given the low slopes (5°–19°) on Hawaiian volcanoes [*Iverson*, 1995], although reduced shear strength within the edifice due to the presence of dense, hot cumulate rocks [*Clague and Denlinger*, 1994; *Johnson*, 1995] could allow for high deformation rates. Alternatively, additional forces causing or contributing to flank motion could be possible. Other potential driving forces for the observed rapid deformation include forceful dike intrusions into the volcano's rift zones [*Swanson et al.*, 1976] and overpressurization of magma stored within the rift zones [*Delaney et al.*, 1990; *Delaney et al.*, 1998; *Delaney and Denlinger*, 1999; *Cayol et al.*, 2000].

[3] In addition to flank instability, inflation and deflation of Kīlauea's summit and upper rift zones result from magma accumulation in and withdrawal from subsurface reservoirs.

Additional supporting information may be found in the online version of this article

[1]University of Miami, Rosenstiel School of Marine and Atmospheric Sciences, Marine Geology and Geophysics, Coral Gables, Florida, USA.
[2]Florida Atlantic University, Department of Civil, Environmental, and Geomatics Engineering, Fort Lauderdale, Florida, USA.
[3]Now at Ludwig-Maximilians University of Munich, Department of Earth and Environmental Sciences, Munich, Germany.
[4]Utrecht University, Department of Earth Sciences, Utrecht, Netherlands.
[5]Hawaiian Volcano Observatory, United States Geological Survey, Hawai'i, USA.

Corresponding author: C. Plattner, Ludwig-Maximilians University of Munich, Department of Earth and Environmental Sciences, Munich, Germany. (christina.plattner@iaag.geo.uni-muenchen.de)

2169-9313/13/10.1002/jgrb.50194

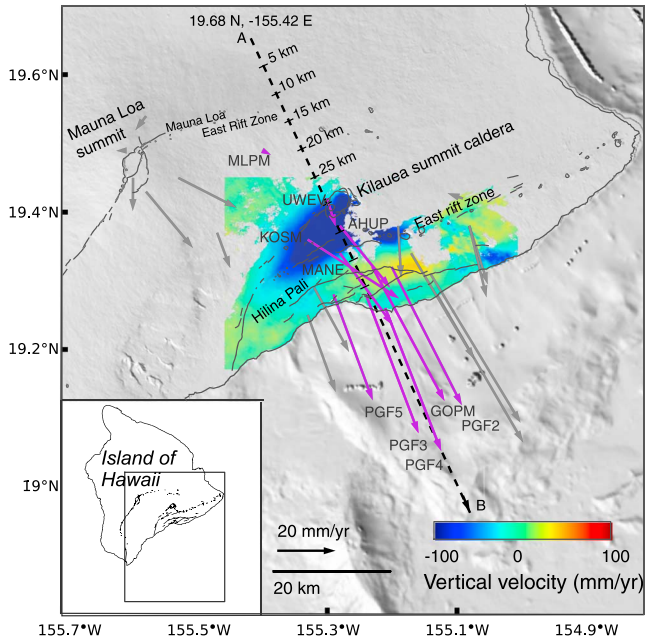

Figure 1. Vertical surface velocities from InSAR time series analysis showing an elliptical region of subsidence centered at Kīlauea's summit and upper rift zones. Horizontal GPS velocities indicate seaward motion of Kīlauea's south flank. GPS sites shown in purple were used for two-dimensional finite element model evaluation along (dashed line) profiles a–b. Shaded relief of Hawai'i Island is from the Shuttle Radar Topography Mission. Faults are shown as dark gray lines and taken from U. S. Geological Survey database (http://earthquakes.usgs.gov/regional/qfaults).

During periods of no intrusions, steady eruptive activity, and constant magma supply, the summit is characterized by subsidence with rates of ~ 6–8 cm/yr [*Delaney et al.*, 1993; *Cervelli and Miklius*, 2003; *Poland et al.*, 2012; *Baker and Amelung*, 2012]. The kinematics of flank motion and summit subsidence have been investigated using elastic half-space dislocation modeling. Horizontal surface displacements on the flank have been interpreted as due to ~ 20–28 cm/yr slip along the deep (~ 8–12 km) subhorizontal décollement fault coupled with deep (~ 6–10 km) rift opening (both model components are required for the volcano's north flank to remain fixed), with an opening volume equivalent to 0.025–0.06 km^3/yr [*Delaney et al.*, 1993; *Owen et al.*, 1995; *Cayol et al.*, 2000; *Owen et al.*, 2000a]. Models that include deep rift opening also fit the broad area of summit and upper rift zone subsidence. An alternative explanation for summit subsidence is volume loss from a shallow magma reservoir at 2–4 km depth [*Delaney et al.*, 1993; *Cervelli and Miklius*, 2003]. Gravity change during periods of summit deflation indicates only minor magma withdrawal, however, suggesting that sagging related to rift zone opening is an important mechanism for summit subsidence [*Johnson*, 1987; *Johnson*, 1992; *Kauahikaua and Miklius*, 2003; *Johnson et al.*, 2010].

[4] Geodetic time series provide the best means of assessing the characteristics of Kīlauea's deformation field. Since the onset of the Pu'u Ō'ō-Kuapaianaha eruption in 1983 [*Heliker and Mattox*, 2003], horizontal flank motion rates along the volcano's southern coastline have been relatively steady at ~ 6–8 cm/yr [*Delaney et al.*, 1990; *Miklius et al.*, 2005]. Prior to the start of that eruption, however, intrusions and short-lived eruptions were much more frequent [*Dzurisin et al.*, 1984; *Cayol et al.*, 2000], and deformation from transient tectonic and magmatic events was superimposed on the flank motion signal [*Swanson et al.*, 1976]. For example, following the 1975 *M*7.2 Kalapana earthquake, horizontal deformation rates reached 40 cm/yr [*Delaney and Denlinger*, 1999]. During 1983–2003, however, changes in the rate and style of deformation were the exception. Leveling, GPS, and interferometric synthetic aperture radar (InSAR) indicated ~ 6–8 cm/yr subsidence at the summit, interrupted only by episodic inflation and deflation events associated with magma accumulation and withdrawal from subsurface magma reservoirs [*Delaney et al.*, 1998; *Delaney et al.*, 1993; *Owen et al.*, 1995; *Cervelli and Miklius*, 2003; *Poland et al.*, 2012; *Baker and Amelung*, 2012]. GPS stations on Kīlauea's south flank show steady velocities over much of that time period [*Miklius et al.*, 2005; *Poland et al.*, 2012] except during occasional dike intrusions and aseismic slip events [e.g., *Montgomery-Brown et al.*, 2010]. The continuity of flank deformation during periods of summit deflation and east rift zone dike intrusions suggests that gravity is a substantial driving force for flank motion [*Delaney et al.*, 1990].

[5] Using deformation data from 2000 to 2003—a time period of low transient tectonic and magmatic activity—we test whether motion of Kīlauea's south flank can be modeled as a "secular" (continuous) gravitational spreading that is modulated by intrusions and/or earthquake events. Few intrusive and earthquake events occurred during this time span, the east rift zone eruption was steady, and little mass change beneath the summit was recorded by gravity surveys [*Cervelli and Miklius*, 2003; *Kauahikaua and Miklius*, 2003; *Johnson et al.*, 2010]. We use numerical modeling to determine the contribution of gravity forces to horizontal and vertical surface velocities, ignoring possible contributions of magmatic pressures and volume changes. We find that gravity-only models can reproduce the principal observation pattern if we incorporate a regional décollement fault and a low viscosity cumulate body at intermediate depth within the volcano.

2. Structure of the South Flank

[6] The basal décollement beneath Kīlauea marks the interface between the volcanic pile and the underlying oceanic crust, and seismic refraction data suggest a depth of 8–12 km and a dip toward the island of about 2° [*Zucca and Hill*, 1980]. Two secondary fault systems have developed in response to the flank motion and strike parallel to the rift zones and coastline; the inward-dipping Koa'e fault zone and the seaward-dipping Hilina fault zone (Figure 1). During the time period between 2000 and 2003, seismicity along the décollement occurred primarily along a ~10 km long segment seaward of the rift zone (Figure 2a). No seismicity is observed farther offshore, although slow-slip events have been documented in this area [*Cervelli et al.*, 2002a; *Brooks et al.*, 2006; *Montgomery-Brown et al.*, 2009; *Syracuse et al.*, 2010]. No major seismicity was recorded during 2000–2003 along the Koa'e and Hilina Pali fault systems.

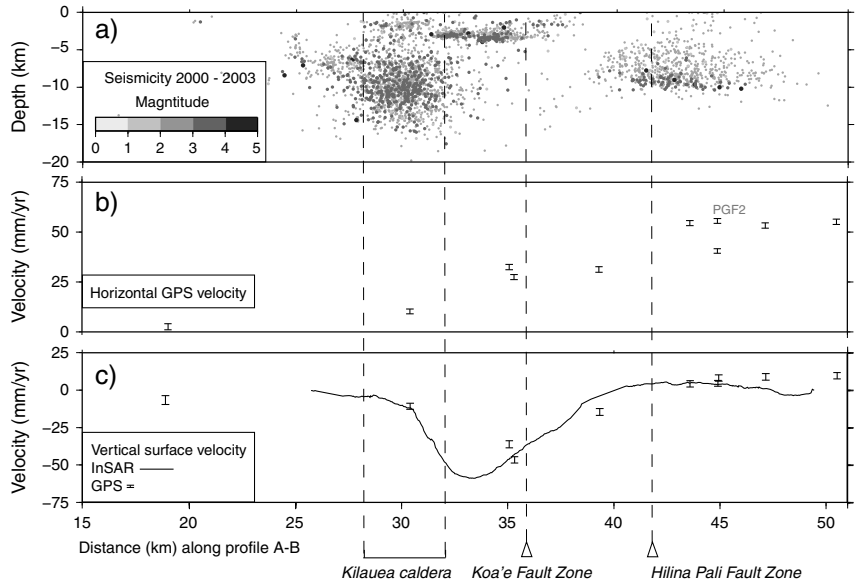

Figure 2. Seismicity and geodetic surface velocities along the subaerial segment of profile A–B (Figure 1) passing through Kīlauea's summit. (a) Earthquakes during 2000–2003 (Advanced National Seismic System Worldwide Earthquake Catalog, Northern California Earthquake Data Center) show seismic events at the décollement (at 39–47 km horizontal distance from Mauna Loa and ~10 km depth), shallow (~1–4 km) seismicity beneath Kīlauea's summit, and a source of seismicity between Mauna Loa and Kīlauea. (b) Horizontal GPS velocity with respect to Mauna Kea (component in direction of profile A–B) increases from Kīlauea's summit to the southeast along the flank (the velocity maximum at site PFG2 (see label) is 53.2 mm/yr). (c) Vertical deformation from (line) InSAR and (points with error bars) GPS indicating subsidence of Kīlauea's summit (maximum subsidence is 58.4 mm/yr).

[7] Magma ascends through a central conduit beneath Kīlauea's summit and is stored in several shallow (1–4 km depth) reservoirs beneath the caldera, from where it can be transported laterally along the east rift zone to feed intrusions and eruptions [*Ryan*, 1988; *Baker and Amelung*, 2012]. Below ~4 km depth, the rift zones are mostly aseismic. One resulting interpretation is that melt is present down to the depth of the basal décollement [*Ryan*, 1988; *Johnson*, 1995]. Seismic and gravity data, however, indicate that the deep rift zone is dense and has high seismic velocities [*Denlinger and Okubo*, 1995; *Okubo et al.*, 1997; *Kauahikaua et al.*, 2000; *Park et al.*, 2009; *Syracuse et al.*, 2010], which argues for the presence of a partial melt-carrying olivine cumulate that experiences ductile deformation [*Clague and Denlinger*, 1994; *Clague et al.*, 1995], which we refer to as a "magma mush."

3. Deformation Data

[8] Deformation of Kīlauea is recorded by InSAR and GPS data acquired between beginning of 2000 and end of 2003. This time period shows little effect of dike intrusions, earthquakes, and slow slip events compared to the following years and thus provides the best estimate of secular flank motion at Kīlauea [*Heliker and Mattox*, 2003; *Miklius et al.*, 2005; *Montgomery-Brown et al.*, 2009; *Poland et al.*, 2012].

3.1. InSAR Data

[9] InSAR time series analysis was completed using two tracks from the Radarsat-1 satellite. Interferograms were generated from one ascending pass (standard beam S3, incidence angle 34–40°) and one descending pass (standard beam S1, incidence angle 24–31°) [*Baker and Amelung*, 2012]. We used the small baseline subset method (SBAS) [*Berardino et al.*, 2002; *Lanari et al.*, 2004] to generate line of sight (LOS) displacement time series for each track [*Baker and Amelung*, 2012]. The overall LOS displacement field can be extracted for any given time period covered by the SBAS time series. The three components of motion (vertical, east, and north) were computed using pairs of ascending and descending LOS displacements [*Wright et al.*, 2004]. Given the viewing geometry of Radarsat-1, the vertical component is well resolved with just one incidence angle from both an ascending and descending pass, while the north component is poorly resolved. For this study, we use only the vertical component computed by extracting the LOS displacements from the time series for the ascending (22 January 2000 to 1 January 2004) and descending (23 January 2000 to 2 January 2004) passes to derive the vertical deformation from 22 January 2000 to 2 January 2004 (Figure 1). Although this period includes a small component of uplift that started in late 2003 [*Poland et al.*, 2012; *Baker and Amelung*, 2012], the dominant subsidence signal during the time spanned is not significantly affected.

3.2. GPS Velocity Data

[10] Global Positioning System (GPS) data are from continuously operating sites on Kīlauea, Mauna Loa, (Figure 1), and Mauna Kea volcanoes and span February 2000 to December 2003. All GPS data were processed using the GIPSY/OASIS II, Release 5.0, software using nonfiducial satellite orbit and clock files provided by the Jet Propulsion Laboratory [*Zumberge et al.*, 1997]. The analysis follows *Sella et al.* [2002], but the daily solutions were aligned to ITRF05 [*Altamimi et al.*, 2007]. From the daily solutions

Table 1. GPS Velocity Data With Respect to a Reference Site on Mauna Kea Calculated for the Time Period Between February 2000 and December 2003

SITE	Longitude	Latitude	d (km)	Velocity East [a] (mm/yr)	Error East[b] (mm/yr)	Velocity North[a] (mm/yr)	Error North[b] (mm/yr)	V_p (mm/yr)	E_p (mm/yr)	Velocity Vertical (mm/yr)	Error Vertical (mm/yr)
MKEA	−155.46	19.80	−15.3	0.0	0.4	0.0	0.2	0.0	0.3	−4.6	0.8
AHUP	−155.27	19.38	35.4	17.2	0.8	−21.2	0.4	26.5	0.5	−46.1	0.7
GOPM	−155.22	19.32	43.7	24.8	0.8	−46.0	0.4	52.2	0.5	4.7	0.7
KOSM	−155.32	19.36	35.2	31.4	0.8	−20.2	0.4	31.6	0.5	−35.7	0.8
MANE	−155.27	19.34	39.4	18.2	0.8	−24.7	0.4	30.1	0.5	−14.1	0.8
MLPM	−155.39	19.49	19.0	2.9	0.9	−1.5	0.4	2.6	0.5	−6.2	1.0
PGF2	−155.19	19.32	45.0	24.1	0.9	−47.5	0.4	53.2	0.5	8.6	0.7
PGF3	−155.23	19.28	47.3	18.1	0.9	−47.7	0.4	50.9	0.5	9.3	0.8
PGF4	−155.20	19.26	50.6	19.2	0.9	−49.0	0.4	52.5	0.5	10.1	0.7
PGF5	−155.28	19.28	45.0	13.5	0.9	−36.4	0.4	38.7	0.5	5.0	0.7
UWEV	−155.29	19.42	30.5	2.9	0.8	−9.5	0.4	9.8	0.5	−10.3	0.7

d is distance in km along profile A–B (Figure 1) for the projected location, V_p is the velocity projected onto the profile A–B (Figure 1) using equation (1), E_p the error for the projected velocity using equation (2).

[a]The horizontal velocity of MKEA ($V_e = -62.8$, $V_n = 34.0$) has been subtracted from all sites to reference velocities to the interior of the island and to eliminate Pacific Plate motion.

[b]The horizontal errors of the ten sites used for the model evaluation are adjusted for error propagation due to referencing.

and error estimates, we calculated velocity and uncertainty for each site by a linear regression that accounts for error estimates by a χ^2-misfit function. Outliers with an offset of more than three times the formal error were not included. Noise within the time series was calculated following *Mao et al*. [1999] and *Dixon et al*. [2000]. We referenced the horizontal GPS velocity data to the stable part of the Island of Hawai'i by subtracting the rate of station Mauna Kea (Table 1), on Mauna Kea, and adjusted all horizontal velocity uncertainty for error propagation. Figure 1 shows the GPS velocities for all sites on Mauna Loa and Kīlauea. The vectors indicate seaward motion of Kīlauea's south flank, with rates up to 60 mm/yr near the coast, while Mauna Loa's flank along its northeast rift zone moves seaward at a rate one order of magnitude less (the velocity of MLPM is less than 3 mm/yr). Mauna Loa's summit shows deformation due to inflation that began in 2002 [*Miklius and Cervelli*, 2003].

3.3. Two-Dimensional Deformation Profile

[11] Our modeling aims to explore the importance of gravity as a driver for deformation of Kīlauea's south flank. We vary structural and rheological initial and boundary conditions to find a good match with horizontal deformation rates. Vertical deformation rates provide a less suitable measure for flank motion, and the observed subsidence signal may be at least partially caused by magma withdrawal from the summit reservoir system [*Cervelli and Miklius*, 2003; *Johnson et al*., 2010]. If the fit is reasonable (similar deformation pattern and amplitude) and the initial and boundary conditions are within realistic bounds, we conclude that gravity body force can be a principal driver of the secular deformation field and that our model parameter choices on the structural and rheological initial and boundary conditions approximate the measured deformation.

[12] We simplify the problem to two dimensions as we are mainly interested in studying the general deformation process. This assumption is justified because the topographic gradient is nearly aligned with the flank motion direction and our profile azimuth, and because the décollement fault surface extends sufficiently in the out-of-plane direction. Our model profile location is chosen to best represent symmetry of flank motion and summit subsidence and therefore extends through Kīlauea's summit along a flank motion parallel cross section at an azimuth of 155° (Figure 1, profile A–B). The location and alignment also maximize the spatial coverage of the InSAR data and passes close to several GPS stations. Conceptual aspects of our model should be applicable to the entire volcano.

[13] We use GPS data from 10 stations that are within 7 km of our model profile (Figure 1 and Table 1) to reduce bias from the three-dimensional geometry of flank motion kinematics. Horizontal velocities and errors are projected onto the profile (Figure 2b), where the projected velocity V_p is calculated by the dot product of the velocity in east (V_e) and north (V_n) direction and the unit vector of the profile azimuth (Table 1):

$$V_p = V_e \times \cos(155^\circ) + V_n \times \sin(155^\circ) \tag{1}$$

[14] We calculated the error in projection direction (E_p) from the major (E_{maj}) and minor (E_{min}) axes of the GPS error ellipse (using the error in east (E_{e}) and north (E_{n}) direction; in our case E_{maj} is always E_{e}) and the angle α (here 65°) between the ellipse major axis (90°) and the profile azimuth (155°) as:

$$E_{\mathrm{p}} = \sqrt{E_{\mathrm{maj}}{}^2 \times \cos^2(\alpha) + E_{\mathrm{min}}{}^2 \times \sin^2(\alpha)} \tag{2}$$

[15] The GPS velocity profile (Figure 2b) shows increasing seaward motion along the flank. The maximum rate is reached at site PGF2 (53.2 mm/yr).

[16] For the vertical deformation profile, we combine data from InSAR and GPS (Figure 2c). The InSAR data are averaged over five adjacent pixels perpendicular to the profile (total width = 200 m) and adjusted to reference the absolute GPS velocities by adding a vertical offset of +1.8 mm/yr. The vertical deformation pattern shows a broad V-shaped subsidence trough along the profile, with the landward slope somewhat steeper than the seaward slope. The maximum subsidence rate along the profile is 58.4 mm/yr.

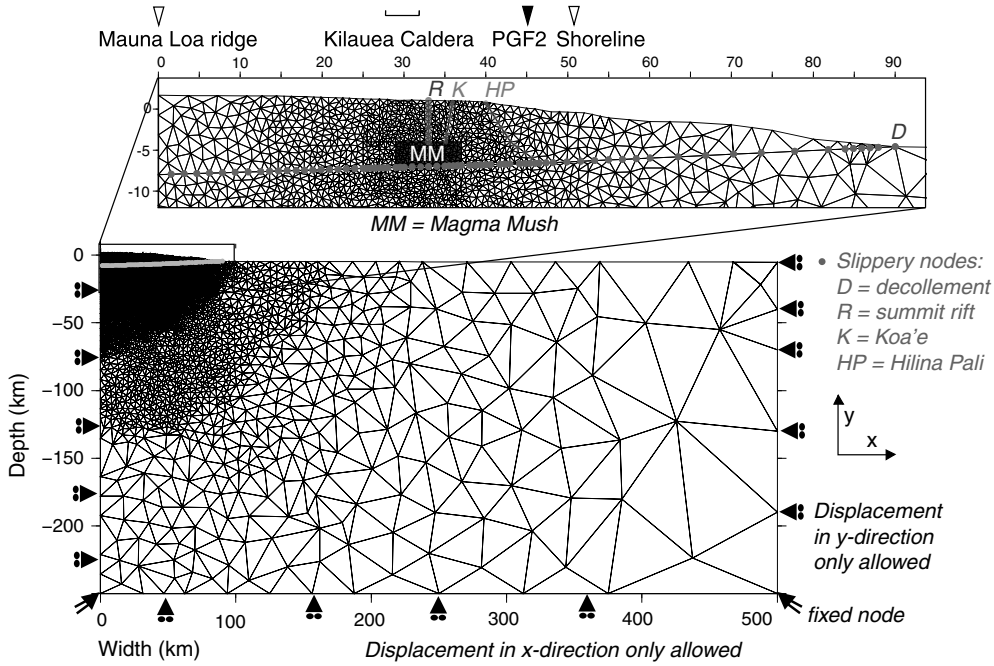

Figure 3. Two-dimensional finite element model geometry showing a cross section from Mauna Loa's north flank, through Kīlauea's summit, to the ocean floor. The nodal displacement boundary conditions are shown along the sides and bottom (italicized). A schematic partial melt-carrying magma-mush zone ("MM") beneath Kīlauea's summit (dark grey-shaded area) is simulated by lower viscosity than the model domain. A fault surface along the décollement (dark gray dots, labeled "D") is implemented using slippery nodes. Additional slippery nodes that are used to test the influence of fault zones and the rift zone are shown in light gray ("R" = summit rift with extension, "K" = Koa'e fault zone with extension and/or normal faulting, "HP" = Hilina Pali fault zone with normal faulting). The locations of Kīlauea Caldera, GPS station PGF2, and the shoreline are indicated above the figure.

4. Deformation Model

[17] We create a two-dimensional mechanical model to simulate gravitational spreading of Kīlauea and assess the surface deformation response. We use the finite element modeling package GTECTON to solve the mechanical equilibrium equation balancing body forces due to gravity and stress gradients, subject to choices of rheology and boundary and initial conditions [*Govers and Wortel*, 1993, 1999]. We assume plane strain to describe the mechanics in a two-dimensional cross section. The model represents the primary structures of the volcano in simplified geometry. We discuss the influence of the idealized geometry, secondary structures, as well as material properties in the "model results" section below.

[18] The model geometry (Figure 3) represents a NW-SE cross section through Kīlauea Volcano, which is an extension of the profile shown in Figure 1. The model cross section begins on Mauna Loa's northeast flank (19.66°N, −155.41°E, 1700 m above sea level). The model domain surface follows the topographic (Shuttle Radar Topography Mission) [*Farr and Kobrick*, 2000] and bathymetric (General Bathymetric Chart of the Oceans) data at 30 arcsecond resolution along the profile to a distance of 500 km from Mauna Loa's northeast flank. The lower domain boundary is set at a depth of 250 km (depth is referenced to sea level rather than the surface due to the topographic gradient in our model geometry). The large model dimension ensures that boundary effects are minimized and is not meant to represent the structure of the lithosphere, as time scales and velocities associated with isostatic adjustments are not relevant for this study. The mesh is refined locally around Kīlauea Volcano. Convergence tests showed insensitivity of our numerical results to further grid refinement.

[19] Our model geometry includes the décollement fault at 8 km depth, which extends from beneath Mauna Loa, passes below Kīlauea, and surfaces at a distance of 90 km from the start of the profile (we use a constant dip and neglect any tapering into thrust faults at a distance somewhat shorter than 90 km from the profile start). The fault dip is 2° down toward the island [*Zucca and Hill*, 1980].

[20] The aseismic magma mush zone beneath Kīlauea's summit is represented by a polygon (the rectangular shape is a simple assumption and does not influence the model results) reaching from a depth of 4 km down to the décollement, and it has a lateral extent of 8 km. The location and dimensions are based on constraints on the aseismic zone beneath the east rift zone [*Ryan*, 1988; *Syracuse et al.*, 2010]. We discuss the effect of a wider or narrower extent of the mush zone on the deformation pattern in our model results. We do not include the summit magma reservoir system in the model we present, but we tested for its influence and discuss its potential impact on our model results below.

[21] We ran two sets of models, with and without a vertical rift zone (we place the rift zone seaward adjacent to the south rim of Kīlauea Caldera because of our profile location passing through the summit). The rift zone extends from the

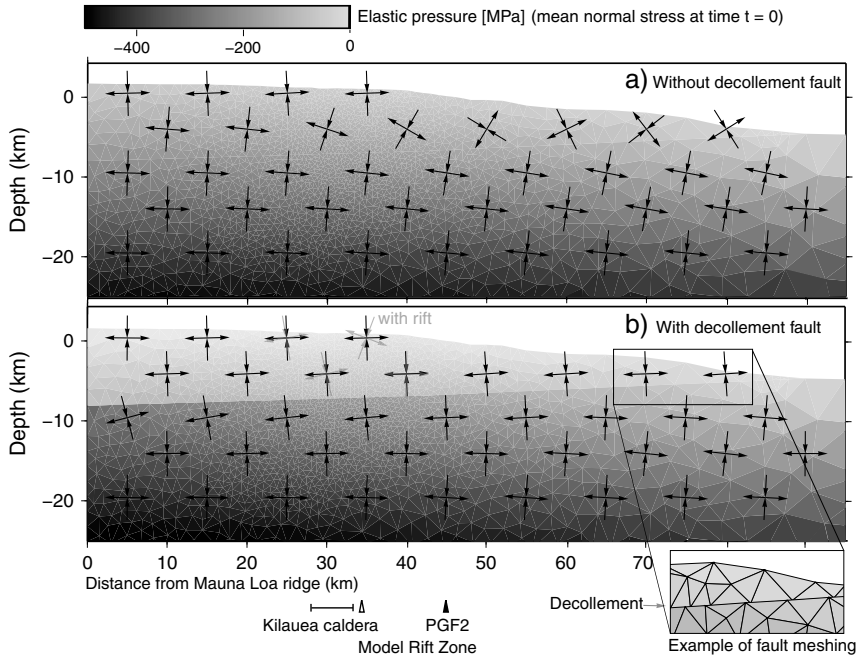

Figure 4. Elastic pressure field calculated as the mean normal stress ($0.5 \times (\sigma_1 + \sigma_2)$) at time step $t = 0$ (supporting information 1); arrows show orientation and direction of principal stresses. (a) Model without the décollement fault. (b) Model with the décollement fault (indicated by boundary between light and dark gray areas) showing significantly reduced stresses in the volcanic pile. An example of the fault meshing and the displaced elements is shown in the lower right corner. The stress axes from a model with a rift are overlain in light gray. The difference between the two model results is only visible in the layer above the décollement between 25 and 40 km horizontal distance. Locations of Kīlauea Caldera, the model rift zone, and GPS station PGF2 are indicated below the figure.

top of magma mush zone to the surface—a vertical distance of 4 km. We also tested models that include flank-cutting normal faults (like the Hilina and Koa'e fault zones) and discuss their influence later.

[22] Gravity body forces are computed from element mass densities and applied as a continuous load throughout the model runtime. The resulting overburden pressure at a given depth beneath the surface of the volcano is higher below the summit than beneath the flanks—in other words, there is a lateral pressure gradient [*Frank*, 1972; *Artyushkov*, 1973; *England and McKenzie*, 1982; *Meijer et al.*, 1997; *England and Molnar*, 1997]. This pressure gradient drives the surface motion that is the primary subject of our investigation. For simplicity, we do not consider the evolution of the volcano here [*McGovern and Solomon*, 1993]. In our model, the horizontal gradients in the gravitational potential energy give a first-order estimate of the surface velocity pattern that develops after a transient relaxation period.

[23] Along the lateral model boundaries, we constrain horizontal motions to be zero, while vertical motion is zero at the 250 km deep base of the model. The lower left and lower right corners of the model are fixed in both dimensions.

[24] The décollement and the Hilina Pali faults are allowed to slip in response to model shear stresses, and the rift zone can open in response to model normal stresses [*Melosh and Williams*, 1989]. For the Koa'e fault zone, we test both dip slip and opening. For simplicity, we assume an absence of fault friction to reduce the number of free model parameters. We discuss the implications of this assumption below.

[25] The model rheology is a Maxwell viscoelastic medium. The volcanic edifice and the underlying crust (which we refer to as host rock or bulk flank) deform elastically over the model time scale. We therefore set the viscosity here to a high value to prevent viscous relaxation on a centennial time scale (host rock viscosity $\eta > 1 \times 10^{23}$ Pa s); here we choose $\eta = 1 \times 10^{30}$ Pa s. We use a Poisson's ratio ν of 0.25, Young's modulus E of 25 GPa (the corresponding shear modulus from $E = 2\mu\ (1+\nu)$ is $\mu = 10$ GPa), and density ρ of 2700 kg/m^3 [*Heap et al.*, 2010, 2011]. Our modeling procedure is to stepwise lower the viscosity of the thermally weakened, partial melt-carrying magma mush by one order of magnitude from 1×10^{30} Pa s in a suite of models until surface velocities comparable to the geodetic data are attained. An estimate of the viscosity is a key result of our work. In the presented models, the magma mush has the same density $\rho = 2700$ kg/m^3 as the host rock, but we also tested the effect of a greater density (3100 kg/m^3) in the magma mush and discuss the results below. Another modification we test and discuss is reduced shear strength due to the presence of a hot magmatic conduit extending from the surface down to the magma mush.

[26] The initial model results from gravity loading of the elastic model. In models with a décollement fault, we use subsequent iterations to allow for relaxation of shear stresses on the fault. The model response after viscous relaxation is computed by time stepping using an unconditionally stable implicit integration scheme (Crank-Nicolson).

Table 2. Maxwell Relaxation Times, Model Time Needed to Fit Geodetic Horizontal Surface Velocity at GPS Site PGF2 (53.2 mm/yr), and Model Horizontal and Vertical Velocity at the Output Time for Viscosities 1×10^{20}–1×10^{16} Pa s (Observed Maximum Vertical Velocity is 58.4 mm/yr)

Viscosity (Pa s)	Maxwell Relaxation Time T (years)	Model Fit Time (t/T)	Model Fit Time (years)	Horizontal Velocity at Fit Time (mm/yr)[a]	Vertical Velocity at Fit Time (mm/yr)
			Model Without Rift		
1×10^{20}	317.1	–	–	–	–
1×10^{19}	31.7	10.5	332.9	53.4	−55.1
1×10^{18}	3.2	23.0	73.6	51.0	−59.9
1×10^{17}	3.2×10^{-1}	35.0	11.2	53.8	−131.7
1×10^{16}	3.2×10^{-2}	45.0	1.4	53.0	−762.1
			Model With Rift[b]		
1×10^{20}	317.1	11	3488.1	55.9	−20.7
1×10^{19}	**31.7**	**286**	**9066.2**	**53.2**	**−8.0**
1×10^{18}	**3.2**	**784**	**2508.8**	**53.2**	**−5.8**
1×10^{17}	$\mathbf{3.2 \times 10^{-1}}$	**1228**	**393.0**	**53.1**	**−5.5**
1×10^{16}	$\mathbf{3.2 \times 10^{-2}}$	**1770**	**56.6**	**53.3**	**−3.2**

[a]Differences in modeled and observed rates of few mm/yr are due to the chosen model output time increments and are not significant.
[b]Model solutions that have reached quasi-steady state are shown in bold.

[27] We selected time step size on the basis of convergence tests where we demonstrated insensitivity to further refinement. All models were run using a time step size of 1/10 the Maxwell relaxation time T of the magma and hot rock reservoir (Table 2). T is a function of the (variable) viscosity η and the (constant) shear modulus μ

$$T = \frac{\eta}{\mu}. \tag{3}$$

[28] We referenced our model results to the time elapsed since the model start t normalized by the Maxwell Relaxation Time T, so that any t/T represents a certain state of stress-relaxation, which is equal for any viscosity. We refer to the normalized time at which the model predictions agree with the observations as the model fit time.

5. Model Results

[29] Below, we describe the viscoelastic deformation response, beginning with the elastic response due to the loading of the model and advancing to viscous flow. We first show the elastic pressure field without and with a free-slipping décollement fault (Figure 4) and the corresponding surface displacement field (Figure 5). Although the elastic deformation field cannot be considered a realistic deformation distribution and does not represent the time-dependent deformation, it provides insight into the effect of the décollement fault and the rift opening on the deformation field. We next discuss the temporal evolution of the horizontal and vertical surface velocity field for models with different magma mush viscosity in order to determine the range of viscosities and model fit times that is consistent with the

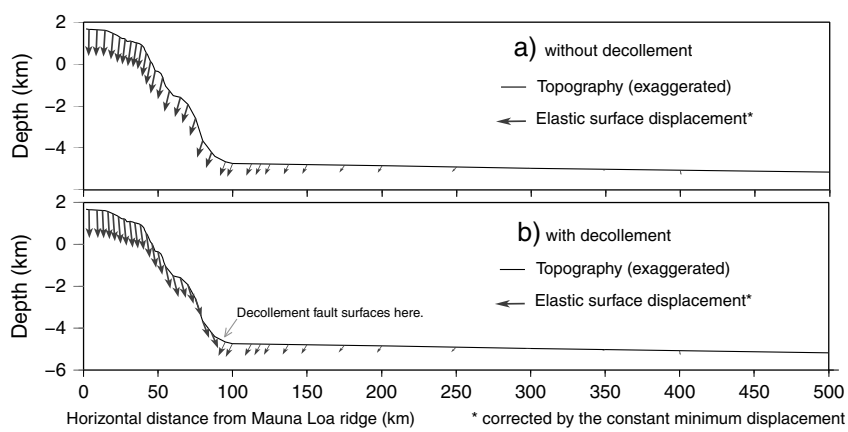

Figure 5. Topographic profile and elastic surface displacement (at time $t = 0$), from which the minimum vertical displacement (at the right side of the model domain boundary at a distance of 500 km from Mauna Loa) has been subtracted for better visibility of the horizontal displacements (which are two order of magnitude smaller than the vertical). As the physical meaning of the elastic displacement magnitude is not relevant, we neglect visualization of the scale. The change in displacement rate follows the topographic gradient to a first order. (a) In the model without a décollement, horizontal displacements are directed inward over the entire left side of the model domain. (b) In the model with a décollement fault, horizontal displacements are directed outward along the flank (transition to inward displacement occurs where the décollement fault reaches the surface). The change in the displacement field due to the presence of a rift zone would not be recognizable in this figure and is therefore not shown.

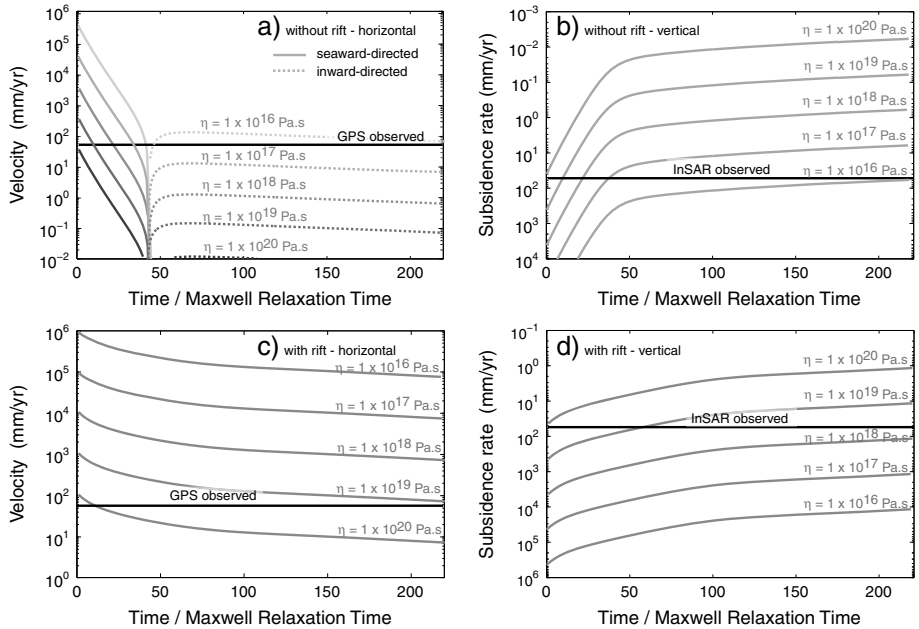

Figure 6. Model surface velocities. (a, c) horizontal velocities at location of GPS site PGF2 and (b, d) maximum vertical velocity (subsidence maximum) for models with different magma mush viscosity and geometry (Figures 6a and 6b: without rift; Figures 6c and 6d: with rift) as function of model time *t/T* and comparison to geodetically observed rates (constant over time). Model velocities are initially high and decrease with time. (Figure 6a) In models without rift zone, horizontal velocities are first directed seaward and decrease rapidly. A reversal in the direction of motion occurs around time $t/T = 50$. Quasi steady state rates, which are directed inward are attained around time $t/T = 75$. (Figure 6b) Vertical velocities show subsidence over the entire model time and converge around $t/T = 75$. (Figure 6c) In the model with the rift zone, horizontal velocities are always directed seaward and reach quasi-steady state around time $t/T = 100$. To fit the GPS rate at any time after quasi-steady state has been attained, a magma mush viscosity lower than $\sim 2.5 \times 10^{19}$ Pa s is required (the lower the viscosity the greater the fit time *t/T*) (Table 2). (Figure 6d) Vertical velocities show subsidence over the entire model time and reach quasi steady state around time $t/T = 100$. For any magma mush viscosity at the time *t/T* at which the horizontal rate is fitted, the subsidence rate is smaller than observed (Table 2). In other words, the lower the magma mush viscosity, the greater the difference between horizontal and vertical deformation rates.

observations (Figure 6). Using a preferred magma mush viscosity and model fit time, we then discuss the spatial pattern of the velocity field at the surface (Figure 7) and within the volcanic edifice (Figure 8). In particular, we discuss the effect of the presence of a rift zone on the deformation behavior and the modeled surface velocity field.

5.1. Elastic Deformation Field

[30] Before viscous relaxation occurs, the imposition of element gravitational stresses (Figure 4) (time $t = 0$) causes compressible elastic deformation with surface subsidence occurring over the entire model domain (Figure 5). The subsidence at any point along the surface is proportional to the gravitational potential energy, which, to first order, follows the topography. The subsidence is therefore highest at Mauna Loa's flank and decreases along the flank of Kīlauea. The elastic displacement causes only minor flattening of the topography and steepening of the décollement fault (the change of only ~1° keeps dip of the décollement fault within the observed range).

[31] The presence of a free-slipping décollement fault induces seaward displacement of the entire Mauna Loa-Kīlauea mass as the décollement fault undergoes (low-angle) thrust motion (Figure 5b). The fault displacement magnitude increases gradually along the flank with distance from the fixed Mauna Loa model domain boundary. As a result of the associated tensional stresses, the pressure is reduced in the flank overlying the décollement fault (Figure 4b; supporting information 1). Principal stress axes rotate to become perpendicular to the frictionless décollement fault [*Mandl*, 1988].

[32] The (initial, elastic) stress and pressure field for a model with rift opening is only slightly different from a model without a rift; hence, we do not display it here. As the rift is not connected to the décollement fault, the horizontal displacement along the rift tapers out at depth.

5.2. Viscous Deformation Field

[33] Following the elastic deformation ($t > 0$), viscous relaxation in the mush zone of the gravity-induced differential stresses and pressure gradients drives deformation at a strain rate that is inversely proportional to the viscosity and proportional to the differential stresses (the deformation pattern is explained below). This implies that surface velocities decrease exponentially with time due to viscous stress relaxation. After an initial period of rapidly decreasing flow velocities, surface velocities become quasi-steady state in our models (Figure 6).

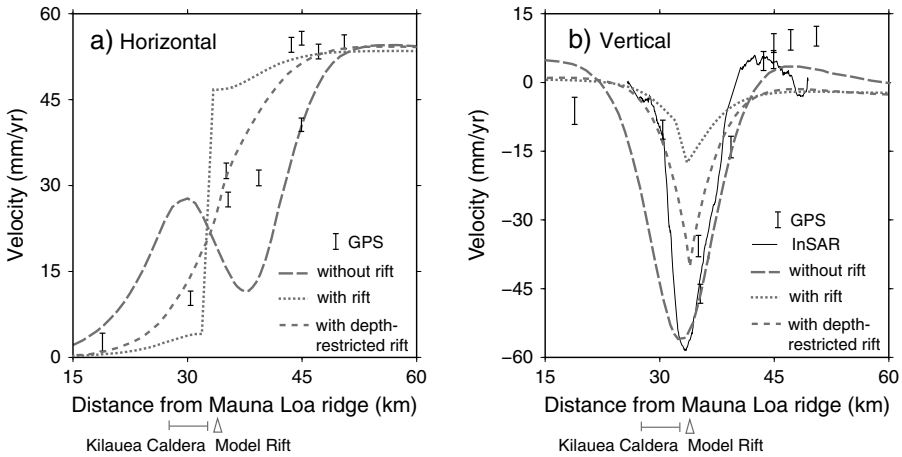

Figure 7. Surface velocities at model fit time for a model without a rift zone, a model with a rift zone, and a hybrid model with a depth-restricted rift zone (in this example the upper 1000 m of the rift are locked), and comparison to geodetic data. All models have a magma mush zone viscosity of $\eta = 1 \times 10^{19}$ Pa s. (a) Horizontal velocities show increasing rates of seaward motion along the flank. The model without a rift zone ($t/T = 10.5$ when horizontal rates are still directed seaward) shows a perturbation caused by the subsidence trough; the model with a rift zone shows a nearly Heaviside function-shaped velocity profile. The model with a depth-restricted rift zone (here 1 km below surface) shows a good fit to the GPS data with a strong gradient across the rift zone. (b) Vertical velocities show a region of subsidence centered south of Kīlauea Caldera (above the model rift zone). In the model without a rift zone, a flexural bulge is located seaward of the trough. In the models with a full or a depth-restricted rift zone, the velocity profiles are steeply V-shaped.

This surface deformation signal results from viscous spreading of the magma mush that causes elastic deformation of the surrounding host rock.

[34] We stepwise lower the viscosity in the magma mush by a factor of 10 from 1×10^{30} Pa s in a suite of models. For magma mush viscosities lower than $\sim 1 \times 10^{21}$ (in models without a rift zone) or 1×10^{22} Pa s (in models with a rift zone), the maximum surface deformation becomes significant on geodetic time scales (> 1 mm/yr). Below, we examine the deformation patterns for models with and without a rift zone in detail. In general, the décollement fault shows differential slip that causes horizontal motion of the south flank, while the north flank remains stable (Figure 7a). High slip rates occur beneath the magma mush and seaward along the south flank, while inward of the mush zone slip rates are low (Figure 8). The surface velocity field shows the development of a subsidence zone above the spreading magma mush (Figure 7b).

[35] We next compare model surface velocities with the GPS observed velocities at two locations along the flank: the site of observed maximum horizontal velocity at GPS site PGF2 (53.2 mm/yr) and of the observed maximum vertical velocity from InSAR near Kīlauea's summit (58.4 mm/yr) (Figure 6). Using these locations, we select the model time that provides the best fit to the observed deformation (Figure 7). If possible, we consider only output times that were equal or greater than the necessary time for the model to reach quasi-steady state. As the observed subsidence rate likely contains an unknown contribution from magma withdrawal of the summit source, our primary constraint for the observed deformation is the horizontal displacement rate. The vertical displacement rate serves as a secondary comparison and allows for speculations on the contribution of flank motion to subsidence versus other sources.

5.2.1. Model Without Rift Opening

[36] Horizontal velocities in this model are zero inward of the magma chamber in Figure 8a. Horizontal viscous stretching of the magma mush facilitates horizontal motions in the region to the right of it above the décollement fault. Horizontal stretching of the magma mush results in thinning and downward motions in the region above it. The top ~4 km of the flank region is entirely elastic and thus responds to magma mush deformation by flexural subsidence. At sufficiently large horizontal distance to the right of the magma mush, velocity gradients go to zero as the entire flank moves seaward over the décollement.

[37] The horizontal velocity at the flank shows a strong variation with time. At early times, the flank undergoes seaward motion (extension), while at $t/T = \sim 50$, a reversal in the direction of motion takes place in response to subsidence in and above the magma mush region (Figure 6a). The geodetic rate can only be fit at a model time at which the model velocities have not yet reached quasi-steady state and horizontal surface velocities are still directed seaward along the flank. While we do not recommend using these solutions for constraining the magma mush viscosity, for completeness, we listed the results in Table 2 and briefly described the velocity field that fits the geodetic data. The model velocity profile shows a steep gradient across Kīlauea's summit and a significant velocity perturbation due to summit subsidence, which is not seen in the GPS data (Figure 7a).

[38] The vertical surface velocity above the magma mush shows subsidence throughout the model run time, and velocities reach quasi-steady state after $t/T = \sim 75$ (Figure 6b). For a magma mush viscosity of 1×10^{19} Pa s, at the model fit time for horizontal rates, the model subsidence is similar to the observed (Table 2). The vertical velocity profile shows flexural subsidence that is almost symmetric (Figure 7b).

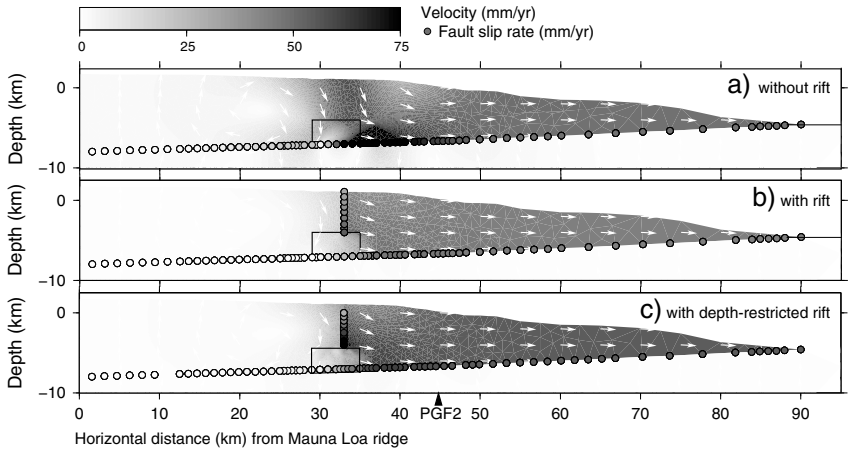

Figure 8. Velocity field by magnitude and with uniform-length arrows showing flow direction and rate of décollement fault slip and rift opening at slippery nodes. Results are from models with magma mush viscosity of 1×10^{19} Pa s at model fit times (Table 2 and Figure 7). (a) Model without rift zone (not in quasi-steady state). (b) The model with a rift zone shows block motion of the south flank. (c) Hybrid model with depth-restricted rift zone (in this example, the upper 1000 m of the rift is locked).

On the seaward side of the subsiding region, a small uplifted bulge is expressed in the modeled surface velocity, which fits the observed signal. Regardless, as the horizontal deformation rates cannot be used to constrain the model results, the model without a rift zone is not suitable for estimating magma mush viscosities.

5.2.2. Model With Rift Opening

[39] Rift zone opening above the gravitationally spreading magma mush allows for flank motion at shallow depths (up to the surface). The entire flank moves seaward, with the velocity controlled by the magma mush viscosity (Figure 6c). The horizontal velocity at the south flank is directed seaward at any time and velocities reach quasi-steady state at $t/T = \sim 100$. The observed horizontal deformation rate at time $t/T = 100$ is fit by a magma mush viscosity of 2.5×10^{19} Pa s (Figure 7a), with lower viscosities fitting at greater t/T (Figure 6a and Table 2). The smaller the viscosity, however, the less constant the surface velocities remain over a given time period (suggesting at least $\sim 2.5 \times 10^{17}$ Pa s to fit the geodetic observations from 2000 to 2003). The horizontal velocity profile is characterized by a Heaviside function across the rift (Figure 7a). Surface velocities and the slip rate of the décollement fault are almost constant along the south flank (block motion); only beneath and immediately seaward of the magma mush do lower rates occur (Figure 8b).

[40] The vertical velocities approach quasi-steady state simultaneously with the horizontal velocities ($t/T = 100$). Fitting the maximum subsidence rate requires a magma mush viscosity of $\sim 4 \times 10^{18}$ Pa s or lower (Figure 6b). For any magma mush viscosity, however, the maximum subsidence rate at the time at which the horizontal rates are fit is smaller than the observed subsidence rate (Table 2). The misfit is greater for lower magma mush viscosities than that for higher viscosities (i.e., lower magma mush viscosities produce less subsidence for equal horizontal velocities along the flank). Using a viscosity of 2.5×10^{19} Pa s, we still obtain only a subsidence rate of 15 mm/yr at the model fit time. We interpret the different surface deformation behavior in this model (with respect to the previous model without a rift) as a result of extensional strain above the magma mush now being accommodated by horizontal displacement at the rift, instead of thinning (subsidence). The shallow subsidence trough is broad, V-shaped, and centered at the location of the rift (Figure 7b).

5.2.3. Hybrid Model With Depth-Restricted Rift Opening

[41] We now test a hybrid rift model in which opening occurs at depth but does not reach the surface. Figures 7a, 7b, and 8c show an example with rift opening restricted to 1 km below the surface. We find that for this depth-restricted rift opening model, the fit of the horizontal velocity field is significantly improved. The model avoids both the subsidence-induced perturbation of the horizontal velocity in the model without a rift zone, as well as the Heaviside function type change in the model with a surface-reaching rift zone. For the vertical deformation pattern, the subsidence trough is V shaped with a maximum rate somewhere between that of the model with full rift zone opening and that without a rift zone (Figure 7b).

5.3. Influence of Model Parameters

[42] Gravitational spreading of the magma mush causes surface deformation regardless of whether the décollement fault is free to slip or locked. If the décollement is locked, spreading rates are lower due to the forces resisting horizontal motion, and flank motion cannot be sustained over long time periods at the observed rate. Locking of the décollement fault on the landward side of the magma mush zone enhances the flank motion slightly relative to a model in which the décollement fault is free to slip along its entire length.

[43] Friction along the décollement fault reduces its slip rate and, by consequence, the surface velocities. Our results thus provide an upper bound on surface velocities for any magma mush viscosity.

[44] A horizontal shift in the location of the rift zone (within an area bounded by the south rim of the caldera and the Koa‘e fault zone) directly influences the lateral locations of the subsidence trough and the sharpest gradient in horizontal velocities but does not influence the deformation rate or style. The location we chose provided the best fit to GPS and InSAR data. Small variations in the dip of the rift zone do not significantly influence the horizontal velocities.

[45] Thus, if we include the steep inward dipping Koa'e fault zone (zero friction) into a model without a rift zone and allow it to open horizontally (cracking), the surface velocities are similar to those of the model with a rift zone. If the model includes a rift zone and the Koa'e fault zone, opening occurs on both structures. If only normal faulting is allowed, subsidence of the hanging wall occurs.

[46] We tested models that include the Hilina Pali normal fault system (zero friction), but the resulting relative motion on both sides of the fault zone (subsidence occurs on the seaward hanging wall) increases the misfit to the observed subsidence pattern. The difference in the horizontal velocity pattern is negligible. This agrees with observations from seismicity that suggest the Hilina Pali fault zone was not moving during the time period of our geodetic observations.

[47] In our models, we assume that the host rock remains fully elastic—i.e., that viscous relaxation of the volcanic flank itself does not contribute to the secular deformation. This choice is motivated by the absence of gradients in the observed flank motion away from the magma mush zone, where motion is block-like.

[48] Similarly, in our models, we neglect viscous deformation of the lithosphere, of which the contribution to the observed surface velocities is minor. We did not test the effect of more complex rheology of the bulk flank (and/or magma mush), including viscoelastoplastic material properties.

[49] We examined the effect of variable material properties on deformation. For example, low elastic moduli (Young's modulus = 10 GPa, Poisson's ratio = 0.15) may be caused by cracking [*Heap et al.*, 2010] at shallow depths (<4 km) above the magma mush zone. Reducing the elastic moduli leads to a narrower subsidence trough and enhances horizontal deformation rates along the south flank, in particular for models without rift zone opening or with a depth-restricted rift zone opening.

[50] A greater density for the magma mush zone relative to the surrounding edifice increases the deformation only slightly, e.g., by ~1 mm/yr for 3100 kg/m^3. We therefore conclude that, to first order, it is the low viscosity and not the high density that drives spreading of the deep olivine cumulate magma mush. Therefore, we did not test the effect of higher density outside of the mush zone beneath the summit and rift zone.

[51] Decreasing the vertical and lateral dimension as well as the depth range of the magma mush within reasonable ranges to fit the seismic velocity anomaly and/or extent of the aseismic zone beneath the east rift zone [*Syracuse et \al.*, 2010] does not significantly influence the results. Additional magma bodies, such as the summit reservoirs beneath the summit caldera, also do not impact our models, probably because of the relatively small size and shallow depths of the magma reservoirs compared to the overall model geometry.

6. Discussion

[52] We have tested viscoelastic models to better understand what drives flank motion and summit subsidence at Kīlauea. The purely elastic model solution ($t = 0$) demonstrates that gravity forces can activate a low-friction décollement fault beneath Mauna Loa and Kīlauea. This model, however, cannot explain extension across and subsidence of Kīlauea's summit, and it does not reproduce the observed contrast in horizontal motion between the mobile south flank and the stable north flank because the two flanks are not sufficiently decoupled, as was found in previous studies using elastic half-space models [*Delaney et al.*, 1993; *Owen et al.*, 1995; *Owen et al.*, 2000a].

[53] The model solutions with viscous flow ($t > 0$) in the magma mush explain decoupling of the south flank from the north flank at Kīlauea at depth. We tested different representations of the shallow rift zone above the magma mush. These are models without and with a rift zone reaching from the magma mush to the surface. We also tested one example of a hybrid model with a depth-restricted rift zone (upper part locked).

[54] Models without a rift zone do a good job of explaining the geodetic observations of broad extension across, and subsidence at, Kīlauea's summit (Figures 7a and 7b). The models without a rift zone even replicate the small uplift adjacent to the subsidence trough on the seaward side of the flank, which is observed in the vertical geodetic velocity data (Figure 7b). The reduction in slip rate along the décollement and within the edifice seaward of the mush (i.e., in the updip direction along the décollement fault from the mush) agrees with the location of a band of microseismicity that has been observed to run parallel to the rift zone [*Brooks et al.*, 2006]. While these models are also most suitable for explaining the deformation pattern from spreading during the time intervals in between shallow magmatic deformation events, they cannot explain sustained flank motion, as after a model run time that is long enough for the model to reach quasi-steady state, the velocities along the flank have reversed to an inward direction. The presented solutions (Figure 7) were taken from a model that did not reach quasi-steady state, and their reliability is therefore somewhat questionable.

[55] In contrast, the model with a rift zone provides a numerically robust solution with horizontal velocities reaching quasi-steady state. This model better approximates the long-term deformation, with flank motion being driven by continuous deformation at depth and compensated in the shallow part of the flank by rift opening. Passive shallow (< 3 km) dike intrusion in response to deeper rift zone extension has been suggested for Kīlauea [*Delaney and Denlinger*, 1999; *Owen et al.*, 2000b; *Cervelli et al.*, 2002b]. Our model, however, simulates rift opening that is continuous over time rather than episodically occurring after time periods during which no dike intrusion events take place. Because we simulate continuous rift opening, the solution shows a discontinuity in the horizontal velocity (not observed in the summit area) and small vertical velocities. A next step in modeling the unstable flank would therefore represent rift zone spreading by episodic dike intrusion.

[56] Here we presented a hybrid model with depth-restricted rift opening (upper part locked) that provides perhaps the best fit to the observations. It is associated with a more realistic horizontal velocity pattern than the two end-member models (Figure 7a) and a summit subsidence rate between the two other models (Figure 7b).

[57] The primary conclusion of our work here is that gravity forces are sufficient to explain the observed surface deformation. This does not mean that we exclude the possibility of other contributions to the deformation field. Although we believe that gravity is a dominant driver, the relaxation due to magmatic stresses (for instance) may also contribute to the observed velocity field.

[58] An exact determination of the viscosity of the magma mush zone is not possible because the age and size of the body and its stress relaxation state, particularly with respect to previous transient events (like dike intrusions), are unknown. We therefore cannot constrain the time scale of the viscous relaxation. We can, however, argue for a viscosity somewhere in-between the range of 2.5×10^{19} Pa s and $\sim 2.5 \times 10^{17}$ Pa s. Higher viscosities yield lower quasi steady state velocities than observed, while for lower viscosities, the quasi steady state velocity would decrease significantly over a time period of 4 years (because of the smaller the Maxwell relaxation time). Thus, higher viscosities (2.5×10^{19} Pa s) better explain constant, secular rates. Our model results generally agree with flank viscosity estimates of 2×10^{19} Pa s by *Delaney and Denlinger* [1999], if we consider their value as representative of the magma mush zone (their calculation did not consider heterogenous material properties along the flank, while our model requires a somewhat lower viscosity in the magma mush zone compared to that of the bulk flank in order to allow decoupling).

[59] Our models provide some constraints on the mechanisms that contribute to summit subsidence. Models with rift zone opening (both surface-reaching and depth-restricted) have subsidence rates of up to two thirds of the observed rate (Figure 7b and Table 2, depending on the magma mush viscosity). That gravitational, viscous spreading of the magma mush (rifting) cannot explain all the observed subsidence is consistent with previous studies [*Johnson*, 1992; *Cervelli and Miklius*, 2003; *Johnson et al*., 2010]. These studies suggest that summit subsidence during periods of steady state eruptive activity (i.e., constant magma supply, no rift zone intrusions, and no change in the effusion rate at the eruption site) is caused by a combination of spreading and magma reservoir contraction. The contraction may be a consequence of cooling and crystallization of stored magma [e.g., *Johnson*, 1992], but is more likely a result of magma withdrawal from the reservoir located beneath the seaward part of Kīlauea Caldera [e.g., *Cervelli and Miklius*, 2003; *Baker and Amelung*, 2012] as supported by mass loss modeled from gravity measurements [*Johnson*, 1992; *Kauahikaua and Miklius*, 2003; *Johnson et al*., 2010]. The relative contributions of the two processes in the summit area are difficult to determine given the simplified nature of our model. Our results suggest that spreading may account for half to two thirds of the observed summit subsidence, consistent with gravity results [e.g., *Johnson et al*., 2010]. In the upper southwest rift zone, where there is less evidence for magma withdrawal, spreading may account for an even larger portion of the observed subsidence.

7. Conclusion

[60] Gravitational spreading of a deep, thermally weakened or partial melt-carrying olivine cumulate, with an average viscosity that is lower than the viscosity of the surrounding host rock, causes subsidence and extension at Kīlauea's summit and seaward motion of the volcano's south flank. The viscosity of the cumulate mush is a critical parameter, as variable densities only cause only minor changes in the deformation rate (~1 mm/yr). Viscous flow allows for lateral decoupling of the south flank from the north flank at depth, while the basal décollement fault provides for vertical decoupling of the volcano from the underlying crust [*Borgia et al*., 2000]. If gravitational spreading of the magma mush and seaward motion of the south flank along the décollement fault are not accommodated by rift zone opening above the magma mush at shallow depths, Kīlauea's summit undergoes broad subsidence. In this case, however, the horizontal flank motion cannot be sustained over long time periods. Passive rift zone opening above the magma mush is therefore necessary to accommodate surface extension and also allows for high rates of horizontal flank motion. Rift zone opening from this deep magma mush zone should not be interpreted as magmatic dike intrusions being fed from the deep mush, as magma storage at Kīlauea takes place at shallower depths (~ 2–4 km), and the magma plumbing system geometry is more complex than we model [*Ryan*, 1988; *Poland et al*., 2012; *Baker and Amelung*, 2012]. Our modeling demonstrates that flank motion at Kīlauea does not require magmatic overpressure in the rift zone. We are hopeful that this result provides a foundation for future studies of volcano flank instability, which can lead to a better understanding of the mechanisms that drive aseismic slip, large earthquakes, and catastrophic collapse.

[61] **Acknowledgments.** The SAR data were provided by the Canadian Space Agency through the Alaska Satellite Facility and the Geohazard Supersite. The GPS network is operated in collaboration by the USGS, Stanford University, and Pacific GPS Facility at the University of Hawai'i. GPS data were provided through the Unavco Facility with support from the National Science Foundation (NSF) and National Aeronautics and Space Administration (NASA) under HSF Cooperative Agreement EAR-0735156. This study was supported by grants from NASA (NNX09AK72G) and the National Science Foundation (EAR1019847) to FA. We thank J. Morgan, R.P. Denlinger, and our anonymous reviewers for helpful comments that improved this manuscript. Guoqing Lin, Marco Bagnardi, Yan Lavallee, Don Dingwell, Khaled Sobhan, and above all USGS Hawaiian Volcano Observatory (HVO) staff, in particular Don Swanson, Jim Kauahikaua, Paul Okubo, and Frank Trusdell are thanked for fruitful discussions on Kīlauea's structure and flank motion dynamics, seismic tomography, magma rheology, and slope instabilities.

References

Altamimi, Z., X. Collilieux, J. Legrand, B. Garayt, and C. Boucher (2007), ITRF2005: A new release of the International Terrestrial Reference Frame based on time series of station positions and Earth orientation parameters, *J. Geophys. Res.*, *112*, B09401, doi:10.1029/2007JB004949.

Artyushkov, E. V. (1973), Stresses in the lithosphere caused by crustal thickness inhomogeneities, *J. Geophys. Res.*, *78*, 7675–7708.

Baker, S., and F. Amelung (2012), Top-down inflation and deflation at the summit of Kīlauea Volcano, Hawaii observed with InSAR, *J. Geophys. Res.*, *117*, B12406, doi:10.1029/2011JB009123.

Berardino, P., G. Fornaro, R. Lanari, and E. Sansosti (2002), A new algorithm for surface deformation monitoring based on small baseline differential SAR interferograms, *IEEE Trans. Geosci. Remote Sens.*, *40*, 2375–2383, doi:10.1109/TGRS.2002.803792.

Borgia, A., P. T. Delaney, and R. P. Denlinger (2000), Spreading volcanoes, *Annu. Rev. Earth Planet. Sci.*, *28*, 539–570, doi:10.1146/annurev.earth.28.1.539.

Brooks, B. A., J. H. Foster, M. Bevis, L. N. Frazer, C. J. Wolfe, and M. Behn (2006), Periodic slow earthquakes on the flank of Kīlauea volcano, Hawai`i, *Earth Planet. Sci. Lett.*, *246*, 207–216, doi:10.1016/j.epsl.2006.03.035.

Cayol, V., J. H. Dietrich, A. T. Okamura, and A. Miklius (2000), High magma storage rates before the 1983 eruption of Kīlauea, Hawai`i, *Science*, *288*, 2343–2346, doi:10.1126/science.288.5475.2343.

Cervelli, P., and A. Miklius (2003), The shallow magmatic system of Kīlauea Volcano, in *The Pu`u `O`o-Kupaianaha Eruption of Kīlauea Volcano, Hawai`i: The First Twenty Years*, U.S. Geol. Surv. Prof. Pap., 1676, edited by C. Heliker, D. A. Swanson, and T. J. Takahashi, pp. 149–164, U.S. Geological Survey, Reston, Virginia.

Cervelli, P., P. Segall, K. Johnson, M. Lisowski, and A. Miklius (2002a), Sudden aseismic fault slip on the south flank of Kīlauea Volcano, *Nature*, *415*, 1014–1018, doi:10.1038/4151014a.

Cervelli, P., P. Segall, F. Amelung, H. Garbeil, C. Meertens, S. Owen, A. Miklius, and M. Lisowski (2002b), The 12 September 1999 Upper East Rift Zone dike intrusion at Kīlauea Volcano, Hawaii, *J. Geophys. Res.*, *107*(B7), 2150, doi:10.1029/2001JB000602.

Clague, D. A., and R. P. Denlinger (1994), Role of olivine cumulates in destabilizing the flanks of Hawaiian volcanoes, *Bull. Volcanol.*, *56*, 425–434, doi:10.1007/BF00302824.

Clague, D. A., J. G. Moore, J. E. Dixon, and W. B. Friesen (1995), Petrology of submarine lavas from Kīlauea's Puna Ridge, Hawai`i, *J. Petrol.*, *36*, 299–349, doi:10.1093/petrology/36.2.299.

Delaney, P. T., and R. P. Denlinger (1999), Stabilization of volcanic flanks by dike intrusion: An example from Kīlauea, *Bull. Volcanol.*, *61*, 356–362, doi:10.1007/s004450050278.

Delaney, P. T., R. S. Fiske, A. Miklius, A. T. Okamura, and M. K. Sako (1990), Deep magma body beneath the summit and rift zones of Kīlauea Volcano, Hawaii, *Science*, *247*, 1311–1316, doi:10.1126/science.247.4948.1311.

Delaney, P. T., A. Miklius, T. Arnadottir, A. T. Okamura, and M. K. Sako (1993), Motion of Kīlauea volcano during sustained eruption from the Pu'u 'O'o and Kupai'anaha Vents, 1983–1991, *J. Geophys. Res.*, *98*, 17,801–17,820, doi:10.1029/93JB01819.

Delaney, P. T., R. P. Denlinger, M. Lisowski, A. Miklius, P. G. Okubo, A. T. Okamura, and M. K. Sako (1998), Volcanic spreading at Kīlauea, 1976–1996, *J. Geophys. Res.*, *103*, 18,003–18,023, doi:10.1029/98JB01665.

Denlinger, R. P., and P. Okubo (1995), Structure of the mobile south flank of Kīlauea Volcano, Hawaii, *J. Geophys. Res.*, *100*, 24,499–24,507, doi:10.1029/95JB01479.

Dixon, T. H., M. Miller, F. Farina, H. Wang, and D. Johnson (2000), Present-day motion of the Sierra Nevada block and some tectonic implications for the Basin and Range province, North American Cordillera, *Tectonics*, *19*, 1–24, doi:10.1029/1998TC001088.

Dzurisin, D., R. Y. Koyanagi, and T. T. English (1984), Magma supply and storage at Kīlauea Volcano, Hawaii, 1956–1983, *J. Volcanol. Geotherm. Res.*, *21*, 177–206, doi:10.1016/0377-0273(84)90022-2.

England, P., and D. McKenzie (1982), A thin viscous sheet model for continental deformation, *Geophys. J. R. Astron. Soc.*, *70*, 295–321.

England, P., and P. Molnar (1997), Active deformation of Asia: From kinematics to dynamics, *Science*, *278*, 647.

Farr, T. G., and M. Kobrick (2000), Shuttle radar topography mission produces a wealth of data, *Am. Geophys. Union. EOS*, *81*, 583–585.

Frank, F. (1972), Plate tectonics, the analogy with glacier flow, and isostasy. Flow and fracture of rocks, *Geophys. Monogr. Ser.*, *16*, 285–292.

Govers, R., and M. J. R. Wortel (1993), Initiation of asymmetric extension in continental lithosphere, *Tectonophysics*, *223*, 75–96, doi:10.1016/0040-1951(93)90159-H.

Govers, R., and M. J. R. Wortel (1999), Some remarks on the relation between vertical motions of the lithosphere during extension and the necking depth parameter inferred from kinematic modeling studies, *J. Geophys. Res.*, *104*, 23,245–23,253, doi:10.1029/1999JB900201.

Heap, M. J., D. R. Faulkner, P. G. Meredith, and S. Vinciguerra (2010), Elastic moduli evolution and accompanying stress changes within creasing crack damage: Implications for stress changes around fault zones and volcanoes during deformation, *Geophys. J. Int.*, *183*, 225–236, doi:10.1111/j.1365-246X.2010.04726.x.

Heap, M. J., P. Baud, P. G. Meredith, S. Vinciguerra, A. F. Bell, and I. G. Main (2011), Brittle creep in basalt and its application to time-dependent volcano deformation, *Earth Planet. Sci. Lett.*, *307*, 71–82, doi:10.1016/j.epsl.2011.04.035.

Heliker, C., and T. N. Mattox (2003), The first two decades of the Pu-u O'o-Kupaianaha eruption: chronology and selected bibliography, in *The Pu'u O'o-Kupaianaha Eruption of Kīlauea Volcano, Hawaii: The First 20 Years*, United States Geological Survey Professional Paper 1676, edited by C. Heliker et al., pp. 1–27, U.S. Geological Survey, Reston, Virginia.

Iverson, R. M. (1995), Can magma-injection and groundwater forces cause massive landslides on Hawaiian volcanoes?, *J. Volcanol. Geotherm. Res.*, *66*, 295–308, doi:10.1016/0377-0273(94)00064-N.

Johnson, D. J. (1987), Elastic and inelastic magma storage at Kīlauea Volcano, in *Volcanism in Hawaii*, U.S. Geological Survey Professional Paper 1350, edited by R. W. Decker, T. L. Wright, and P. H. Stauffer, pp. 1297–1306, United States Government Printing Office, Washington, D. C.

Johnson, D. J. (1992), Dynamics of magma storage in the summit reservoir of Kīlauea volcano, Hawaii, *J. Geophys. Res.*, *97*, 1807–1820, doi:10.1029/91JB02839.

Johnson, D. J. (1995), Molten core model for Hawaiian rift zones, *J. Volcanol. Geotherm. Res.*, *66*, 27–35, doi:10.1016/0377-0273(94)00066-P.

Johnson, D. J., A. A. Eggers, M. Bagnardi, M. Battaglia, M. P. Poland, and A. Miklius (2010), Shallow magma accumulation at Kīlauea Volcano, Hawai`i, revealed by microgravity surveys, *Geology*, *38*, 1139–1142, doi:10.1130/G31323.1.

Kauahikaua, J., and A. Miklius (2003), Long-term trends in microgravity at Kīlauea's summit during the Pu`u `O`o-Ku`paianaha eruption, *U.S. Geol. Surv. Prof. Pap.*, *1676*, 165–171.

Kauahikaua, J., T. Hildenbrand, and M. Webring (2000), Deep magmatic structures of Hawaiian volcanoes, imaged by three-dimensional gravity methods, *Geology*, *28*, 883–886, doi:10.1130/0091-7613(2000)28<883:DMSOHV>2.0.CO;2.

Lanari, R., O. Mora, M. Manunta, J. J. Mallorqui, P. Berardino, and E. Sansosti (2004), A small-baseline approach for investigating deformation on full-resolution differential SAR interferograms, *IEEE Trans. Geosci. Remote Sens.*, *42*, 1377–1386, doi:10.1109/TGRS.2004.828196.

Lipman, P. W., J. P. Lockwood, R. T. Okamura, D. A. Swanson, and K. M. Yamashita (1985), Ground deformation associated with the 1975 magnitude-7.2 earthquake and resulting changes in activity of Kīlauea volcano, Hawaii, *U.S. Geol. Surv. Prof. Pap.*, *1276*, 1–45.

Mandl, G. (1988), *Mechanics of tectonic faulting, models and basic concepts*, Developments in Structural Geology 1, edited by H. J. Zwart, 407 pp. Elsevier, Amsterdam, The Netherlands.

Mao, A., C. G. A. Harrison, and T. H. Dixon (1999), Noise in GPS coordinate time series, *J. Geophys. Res.*, *104*, 2797–2816, doi:10.1029/1998JB900033.

McGovern, P. J., and S. C. Solomon (1993), State of stress, faulting, and eruption characteristics of large volcanoes on Mars, *J. Geophys. Res.*, *98*, 23553–23579, doi:10.1029/93JE03093.

McGuire, W. (2006), Lateral collapse and tsunamigenic potential of marine volcanoes, *Geol. Soc. Spec. Pub.*, *269*, 121–140, doi:10.1144/GSL.SP.2006.269.01.08.

Meijer, P., R. Govers, and M. Wortel (1997), Forces controlling the present-day state of stress in the Andes, *Earth Planet. Sci. Lett.*, *148*, 157–170.

Melosh, H. J., and C. A. Jr.Williams (1989), Mechanics of graben formation in crustal rocks: a finite element analysis, *J. Geophys. Res.*, *94*, 13,961–13,973, doi:10.1029/JB094iB10p13961.

Miklius, A., and P. Cervelli (2003), Interaction between Kīlauea and Mauna Loa, *Nature*, *421*, 229, doi:10.1038/421229a.

Miklius, A., P. Cervelli, M. Sako, M. Lisowski, S. Owen, P. Segall, J. Foster, K. Kamibayashi, and B. Brooks (2005), Global Positioning System Measurements on the Island of Hawai`i: 1997 through 2004. *US Geol. Surv. Open File Rep., 2005-1425*, 48 pp.

Montgomery-Brown, E. K., P. Segall, and A. Miklius (2009), Kīlauea slow slip events: Identification, source inversions, and relation to seismicity, *J. Geophys. Res.*, *114*, B00A03, doi:10.1029/2008JB006074.

Montgomery-Brown, E. K., D. K. Sinnett, M. Poland, P. Segall, T. Orr, H. Zebker, and A. Miklius (2010), Geodetic evidence for en echelon dike emplacement and concurrent slow slip during the June 2007 intrusion and eruption at Kīlauea volcano, Hawaii, *J. Geophys. Res.*, *115*, B07405, doi:10.1029/2009JB006658.

Moore, J. G., D. A. Clague, R. T. Holcomb, P. W. Lipman, W. R. Normark, and M. E. Torresan (1989), Prodigious submarine landslides on the Hawaiian ridge, *J. Geophys. Res.*, *94*, 17465–17484, doi:10.1029/JB094iB12p17465.

Moore, J. G., W. R. Normark, and R. T. Holcomb (1994), Giant Hawaiian underwater landslides, *Science*, *264*, 46–47, doi:10.1126/science.264.5155.46.

Okubo, P. G., H. M. Benz, and B. A. Chouet (1997), Imaging the crustal magma sources beneath Mauna Loa and Kīlauea volcanoes, Hawaii, *Geology*, *25*, 867–870, doi:10.1130/0091-7613.

Owen, S., P. Segall, J. Freymueller, A. Miklius, R. Denlinger, T. Arnadottir, M. Sako, and R. Burgmann (1995), Rapid deformation of the South Flank of Kīlauea Volcano, Hawai`i, *Science*, *267*, 1328–1332, doi:10.1126/science.267.5202.1328.

Owen, S., P. Segall, M. Lisowski, A. Miklius, R. Denlinger, and M. Sako (2000a), Rapid deformation of Kīlauea Volcano: Global Positioning System measurements between 1990 and 1996, *J. Geophys. Res.*, *105*, 18,983–18,998, doi:10.1029/2000JB900109.

Owen, S., P. Segall, M. Lisowski, A. Miklius, M. Murray, M. Bevis, and J. Foster (2000b), January 30, 1997 eruptive event on Kīlauea Volcano, Hawaii, as monitored by continuous GPS, *Geophys. Res. Lett.*, *27*(17), 2757–2760, doi:10.1029/1999GL008454.

Park, J., J. K. Morgan, C. A. Zelt, and P. G. Okubo (2009), Volcanotectonic implications of 3-D velocity structures derived from joint active and passive source tomography of the island of Hawaii, *J. Geophys. Res.*, *114*, B09301, doi:10.1029/2008JB005929.

Poland, M. P., A. Miklius, A. J. Sutton, and C. R. Thornber (2012), A mantle-driven surge in magma supply to Kīlauea Volcano during 2003–2007, *Nat. Geosci.*, *5*, 295–300, doi:10.1038/ngeo1426.

Ryan, M. P. (1988), The mechanics and three-dimensional internal structure of active magmatic systems: Kīlauea Volcano, Hawaii, *J. Geophys. Res.*, *93*, 4213–4248, doi:10.1029/JB093iB05p04213.

Sella, G. F., T. H. Dixon, and A. L. Mao (2002), REVEL: A model for recent plate velocities from space geodesy, *J. Geophys. Res.*, *107*(B4), 2081, doi:10.1029/2000JB000033.

Swanson, D. A., W. A. Duffield, and R. S. Fiske (1976), Displacement of the south flank of Kīlauea volcano: The result of forceful intrusion of magma into the rift zones, *U.S. Geol. Surv. Prof. Pap., 963*, 39 pp.

Syracuse, E. M., C. H. Thurber, C. J. Wolfe, P. G. Okubo, J. H. Foster, and B. A. Brooks (2010), High-resolution locations of triggered earthquakes and tomographic imaging of Kīlauea Volcano's south flank, *J. Geophys. Res.*, *115*, B10310, doi:10.1029/2010JB007554.

Wright, T. J., B. E. Parsons, and Z. Lu (2004), Toward mapping surface deformation in three dimensions using InSAR, *Geophys. Res. Lett.*, *31*, L01607, doi:10.1029/2003GL018827.

Zucca, J. J., and D. Hill (1980), Crustal structure of the southeast flank of Kīlauea Volcano, Hawai`i from seismic refraction measurements, *Bull. Seismol. Soc. Am.*, *70*, 1149–1159.

Zumberge, J. F., M. B. Heflin, D. J. Jefferson, M. M. Watkins, and F. H. Webb (1997), Precise point positioning for the efficient and robust analysis of GPS data from large networks, *J. Geophys. Res.*, *102*, 5005–5017, doi:10.1029/96JB03860.